


ARTICLE

DOI: 10.1038/s41467-017-00855-3

OPEN

Late Holocene slowdown of the Indian Ocean Walker circulation

Mahyar Mohtadi¹, Matthias Prange¹, Enno Schefuß¹ & Tim C. Jennerjahn ²

Changes in tropical zonal atmospheric (Walker) circulation induce shifts in rainfall patterns along with devastating floods and severe droughts that dramatically impact the lives of millions of people. Historical records and observations of the Walker circulation over the 20th century disagree on the sign of change and therefore, longer climate records are necessary to better project tropical circulation changes in response to global warming. Here we examine proxies for thermocline depth and rainfall in the eastern tropical Indian Ocean during the globally colder Last Glacial Maximum (19–23 thousand years ago) and for the past 3000 years. We show that increased thermocline depth and rainfall indicate a stronger-than-today Walker circulation during the Last Glacial Maximum, which is supported by an ensemble of climate simulations. Our findings underscore the sensitivity of tropical circulation to temperature change and provide evidence for a further weakening of the Walker circulation in response to greenhouse warming.

¹MARUM-Center for Marine Environmental Sciences, University of Bremen, 28359 Bremen, Germany. ²Leibniz Centre for Tropical Marine Research (ZMT) GmbH, 28359 Bremen, Germany. Correspondence and requests for materials should be addressed to M.M. (email: mmohtadi@marum.de)

The Walker circulations are zonal atmospheric overturning cells over the tropical oceans with long-term mean surface westerlies along the equatorial Indian and easterlies over the equatorial Pacific Ocean. Their changes are closely tied to the monsoon systems, El Niño-Southern Oscillation (ENSO) and the Indian Ocean Dipole Mode (IOD)^{1, 2}. Thus far, studies on the recent development and future projection of the Walker circulations remain contradictory and suggest either a reduced²⁻⁵ or an enhanced⁶⁻⁹ Walker circulation in response to global warming. This controversy mainly arises from the shortness of the instrumental data covering only a few decades, and necessitates records of Walker circulation changes from the geological past to better understand the sensitivity of the Walker circulation and the hydrological cycle to temperature change²⁻⁴.

One of the most prominent periods for this purpose is the globally cooler climate of the Last Glacial Maximum (LGM). A multi-model ensemble of climate simulations suggests a drier-than-today LGM climate of the Indo-Pacific Warm Pool (IPWP)¹⁰, where the ascending branches of the Indo-Pacific Walker cells reside. A relatively dry IPWP during the LGM has been attributed to a slowdown of the Walker circulation¹¹⁻¹³. These studies further indicate that similar to the present-day situation^{14, 15}, records of rainfall and thermocline depth in the eastern tropical Indian Ocean are the most sensitive diagnostic tools to reconstruct past Indian Walker circulation changes. Presently, the most prominent changes in Walker circulation over the Indian Ocean occur during the IOD years, when the circulation weakens (positive IOD events) or strengthens (negative IOD events). In the eastern tropical Indian Ocean, the thermocline shoals and cools while rainfall decreases during the positive IOD events, and vice versa during the negative IOD events¹⁴⁻¹⁶. In contrast, modern observations show that temperature and rainfall in Africa and the western Indian Ocean beneath the poorly-defined descending branch of the Indian Walker cell¹ do not respond consistently to changes in the Walker circulation^{17, 18}. Thus, reconstructing circulation and rainfall in the eastern tropical Indian Ocean is a critical task to evaluate the model performance in simulating the LGM and future changes in the tropical hydrologic cycle.

In this study, we show that the thermocline was deeper and the amount of rainfall was higher in the eastern tropical Indian Ocean during the LGM compared to the late Holocene. In striking agreement with two climate model simulations, our results suggest that the Walker circulation over the Indian Ocean was stronger during the cooler LGM climate. We infer a further weakening of the Walker circulation with increasing global temperatures during the 21st century.

Results

Thermocline reconstruction. Here we present three sea surface temperature (SST) and five thermocline temperature records calculated from shell Mg/Ca of planktic foraminifera at several sites in the eastern tropical Indian Ocean since the LGM (Fig. 1a, Methods and Supplementary Table 1). We make use of the difference between surface and thermocline temperatures (ΔT) to assess the relative depth of the thermocline, with a larger difference indicating a shallower thermocline and vice versa (Fig. 1a, Supplementary Figs. 1-2). The depth of the thermocline in this region is presently controlled by changes in the atmospheric circulation and a sensitive measure of changes in the Walker circulation¹⁴ (Supplementary Figs. 1-2). Similar to the model comparison below, in the following we compare reconstructed average values for the LGM with those of the late Holocene in order to assess changes in the relative strength of the Indian Walker circulation.

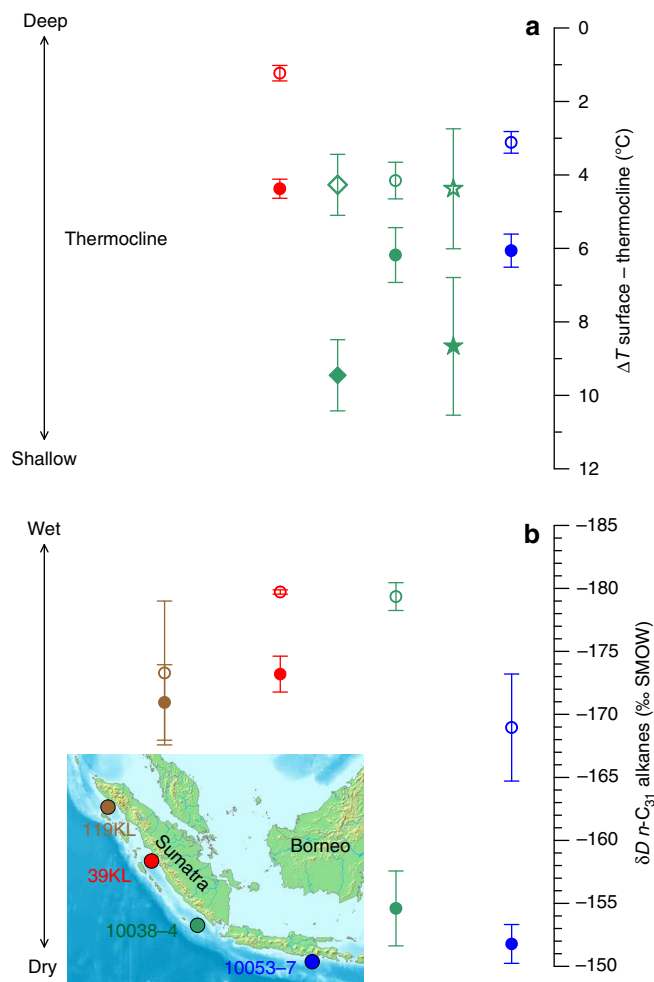


Fig. 1 Depth of the thermocline and amount of rainfall in the eastern tropical Indian Ocean during the LGM and the late Holocene. **a** Average values of the difference between sea surface and thermocline temperatures (ΔT) as a measure of thermocline depth (reverse scale) at three sites. Coloured symbols represent the average values for the late Holocene (filled) and the LGM (open), and correspond to the sites indicated in the inset map. Circles represent the difference between *G. ruber* and *P. obliquiloculata*, stars and diamonds between *G. ruber* and *N. dutertrei* and *G. tumida*, respectively. Vertical bars indicate 95% confidence intervals based on *t*-distributed samples in each time interval (Methods and Supplementary Data 1). The chronology of each period is established independently by ¹⁴C accelerator mass spectrometry dating, each average value comprises a minimum of six samples (Methods, Supplementary Data 1). **b** As in **a** but for the average δD values from plant waxes (*n*-C₃₁-alkanes) by including an additional record (SO189-119KL). LGM values are corrected for relative changes in ice volume (Methods)

Average temperatures for the late Holocene are about 1.5°–3 °C higher at surface but up to 4 °C lower at the thermocline compared to the average LGM temperatures (Supplementary Data 1). The late Holocene ΔT values show a coherent picture regardless of the selected temperature calibration or the time span considered (Fig. 2), and reflect the modern conditions with lower values indicating a relatively deeper thermocline in the non-upwelling region off western Sumatra (site 39KL, Fig. 1a, Supplementary Fig. 2).

Rainfall reconstruction. In order to reconstruct the amount of rainfall over the eastern tropical Indian Ocean, which is another characteristic feature of past changes in the Indian Walker

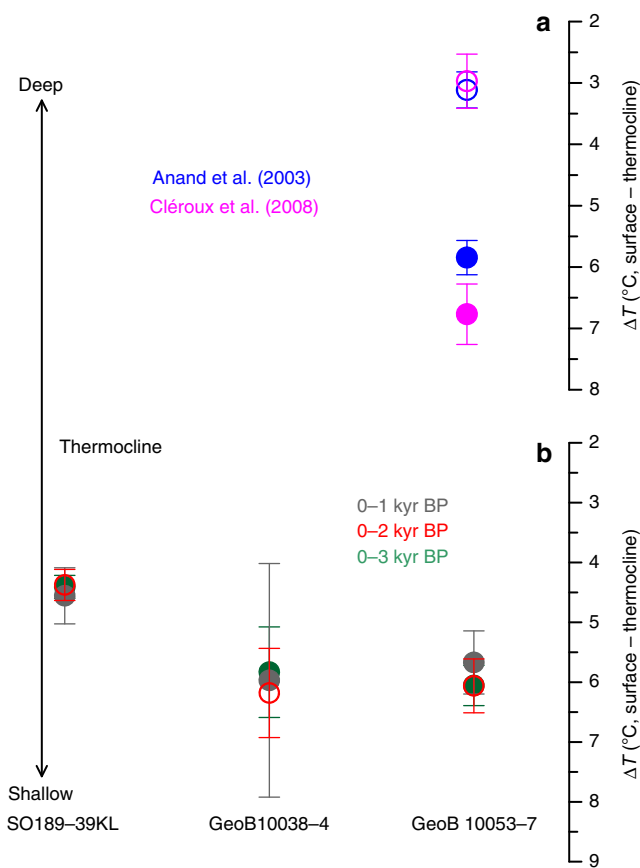


Fig. 2 Comparison between different temperature calibrations and late Holocene intervals. **a** Difference between average surface and thermocline temperatures (ΔT) for the late Holocene (filled circles) and the LGM (open circles) using two different temperature calibrations for *P. obliquiloculata*^{42, 48} indicated by different colours. Vertical bars represent 95% confidence interval based on *t*-distributed samples in each time interval. **b** Average late Holocene difference between surface temperatures derived from Mg/Ca values in *G. ruber* and thermocline temperatures derived from Mg/Ca values in *P. obliquiloculata*. Grey circles (filled) represent ΔT for the past 1000 years, red circles (open) for the past 2000 years and green circles (filled) for the past 3000 years. Vertical bars indicate 95% confidence interval based on *t*-distributed samples in each time interval. Note that the values remain similar regardless of the considered period

circulation^{13, 14}, we analysed the stable hydrogen isotope composition (δD) of terrestrial plant waxes (Fig. 1b). In the tropics, a lower δD of precipitation indicates an increase in the amount of rainfall¹⁹, which is reflected by lower δD values of less degraded plant waxes^{20, 21} in our records (Fig. 3). Our results for the late Holocene corroborate this inference and depict the observed present-day spatial pattern in the amount of rainfall that is highest over central Sumatra and decreases slightly towards the northwest, and considerably towards the southeast (Fig. 1b). We corrected the LGM δD values for global ice volume and exclude any moisture source other than the Indian Ocean²² for our sites (see ‘Discussion’).

Model simulations. The dominant role of equatorial zonal wind anomalies in setting the depth of the thermocline in the eastern equatorial Indian Ocean on glacial–interglacial time scale is corroborated by climate model results. A set of LGM simulations from the Paleoclimate Modelling Intercomparison Project

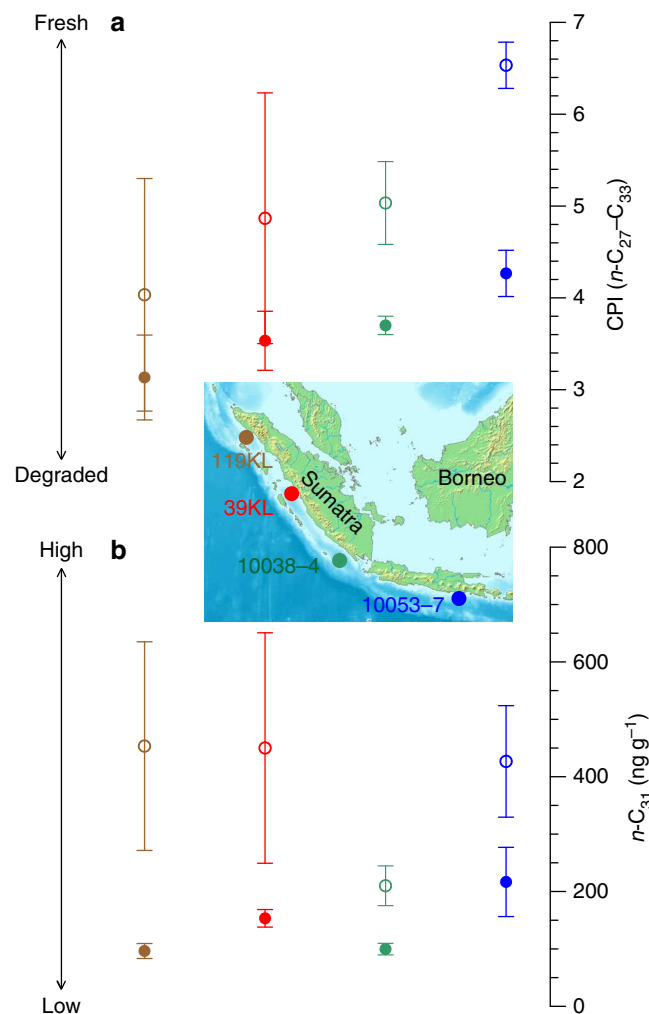


Fig. 3 Late Holocene and LGM concentration of *n*-alkanes and the CPI values in the eastern tropical Indian Ocean. **a, b** Filled and open circles represent average values for the late Holocene and the LGM, respectively. Vertical bars indicate 1σ standard deviation. Note that at all sites, the LGM is characterized by higher sedimentary concentrations of less degraded plant waxes

(PMIP) phases 2 and 3^{10, 23} (<https://pmip2.lscce.ipsl.fr/> and <https://pmip3.lscce.ipsl.fr/>, Supplementary Table 2) suggests an almost one-to-one relationship ($r^2 = 0.81$, $p < 10^{-4}$) between zonal wind anomalies and thermocline depth in the equatorial Indian Ocean (Fig. 4).

Discussion

Our LGM to late Holocene ΔT comparison in the eastern tropical Indian Ocean indicates a considerably deeper thermocline during the LGM and a stronger Walker circulation during a globally cooler climate. Notably, average ΔT values during the LGM are relatively similar at site GeoB 10038-4, regardless of the species used for thermocline temperature reconstruction (green open symbols in Fig. 1a). Modern results based on surface sediments show that the temperature signature carried by thermocline dwellers converge when the thermocline is warmer and deeper, and diverge when the thermocline is shallower and cooler²⁴. Therefore, the similarity between the ΔT values during the LGM additionally supports our inference of a deeper thermocline and a stronger Walker circulation.

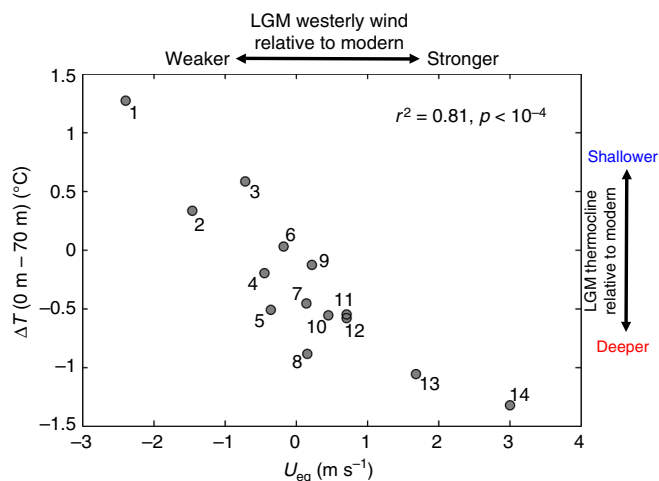


Fig. 4 LGM thermocline depth anomaly in the eastern Indian Ocean vs. equatorial Indian Ocean zonal wind anomaly as simulated in PMIP2 and PMIP3/CMIP5 models. ΔT is used as a measure for thermocline depth and defined as the annual mean temperature difference between surface and 70 m averaged over the eastern Indian Ocean region 4° N– 6° S, 94° E– 104° E. U_{eq} is defined as the annual mean zonal low-level (925 hPa) wind averaged over 5° N– 5° S, 50° E– 100° E (Fig. 5). Shown are LGM anomalies relative to pre-industrial control runs for both quantities. The models are numbered as in Supplementary Table 2. Models with strongest LGM thermocline deepening and westerly wind anomalies are CCSM3 (No. 13) and FGOALS-g1.0 (No. 14)

The southern part of the study area lies within the Australian-Indonesian monsoon realm with an upwelling system that is governed by the seasonally reversing monsoon winds. In this region, dry southeasterly surface winds originating from the high pressure cell over Australia induce seasonal upwelling during boreal summer from June to September. On average, SST drops from mean annual values of ~ 28 to ~ 25 °C during this season, when the mixed layer is only about 20 m thick (World Ocean Atlas 2009²⁵, hereafter WOA09). During the rest of the year, the wind direction is generally reversed and moist air is transported east- and southeastward resulting in downwelling and high SST of >28 °C, a relatively thick mixed layer around 70 m and a deep thermocline (WOA09).

The two southern records of ΔT (sites GeoB10038-4 and 10053-7) lie within the upwelling area of the eastern Indian Ocean and thus, are additionally affected by changes in the meridional Hadley circulation and the southeasterly monsoon winds^{26–29}. Reconstructions of marine productivity that is related to the upwelling intensity in this region^{30, 31} indicate higher productivity during the late Holocene compared to the LGM^{26, 32}. A stronger upwelling and a shallower thermocline in the eastern Indian Ocean during the late Holocene would make the surface cooling more effective and weaken the convective activity and consequently, slowdown the Walker circulation^{1, 13}. This scenario can be best observed presently during the IOD events, when anomalous southeasterly winds shoal the thermocline in this area and weaken the Walker circulation over the Indian Ocean^{1, 14} (Supplementary Figs. 1–2).

The northern part of the study area off west Sumatra lies outside the Australian-Indonesian monsoon realm and is considered a deep tropical non-upwelling region with year-round high rainfall and a deep thermocline (see also ref. 29). As part of the Indo-Pacific Warm Pool, mean annual SST in this region is above 28 °C with little seasonal variability. Observation and model studies show that the thermocline depth and rainfall in the

eastern tropical Indian Ocean are the most sensitive diagnostic tools for detecting changes in the zonal atmospheric circulation and convection in the Indian Ocean, i.e. the Indian Walker circulation¹³. We note that the ΔT results from our site SO189-39KL from a non-upwelling region that is not affected by ocean circulation^{29, 33} indicate that any potential scenario must involve a stronger Walker circulation during the LGM compared to the late Holocene.

We consider the Indian Ocean as the primary moisture source for rainfall at our sites²², both for the late Holocene and the LGM³⁴. The subduction of the Indian Ocean Plate beneath the Sunda Plate forms the ~ 3000 km long and up to 3800 m high volcanic arc mountain chains of the Barisan Mountains in Sumatra to the Priangan and the Dieng Mountains in Java since the Oligocene³⁵. These orographic barriers inhibit the inflow of low-level winds from moisture sources other than the Indian Ocean to the study area. The blocking effect of these mountains is supposed to change only on tectonic timescales, i.e. millions of years, rendering changes in the moisture source of this region during the LGM unlikely.

Our δD results from four sites that lie beneath the ascending branch of the Indian Walker circulation suggest a higher rainfall amount during the LGM compared to the late Holocene (Fig. 1b), and are consistent with another regional δD reconstruction³⁴. Furthermore, the higher concentrations of less degraded plant waxes in the LGM samples (Fig. 3, Supplementary Data 1) suggest a higher supply of plant debris in the LGM compared to the late Holocene and indicate a higher vegetation cover and/or discharge into the ocean. In combination, these findings indicate higher rainfall over the eastern tropical Indian Ocean and combined with a deeper thermocline, a stronger Walker circulation over the Indian Ocean during the LGM compared to the late Holocene. It is noteworthy that the spatial pattern of change in our δD and ΔT records, with a similar sign of change at all sites but with the highest rate of change off southwest Sumatra resembles hydrological changes related to ENSO and IOD, when substantial changes in the Indian Walker circulation occur (Supplementary Fig. 1).

In the two glacial climate model simulations with maximum westerly surface wind anomalies along the equatorial Indian Ocean (CCSM3 and FGOALS-g1.0) the deepening of the thermocline is sufficiently strong to induce warmer-than-today eastern equatorial Indian Ocean subsurface temperatures in the LGM (Supplementary Fig. 3), consistent with our proxy records, while LGM subsurface cooling in the eastern Indian Ocean is simulated by the other models (not shown). The westerly wind anomalies are associated with a strengthening of the Indian Walker circulation implying anomalous ascent of air over the eastern equatorial Indian Ocean and anomalous subsidence over the western portion (Fig. 5), in accordance with our records from the eastern tropical Indian Ocean (Fig. 1). An anti-correlation of the zonal surface wind anomalies with upper-tropospheric zonal wind anomalies aloft ($r^2 = 0.55$, $p < 10^{-2}$) confirms the involvement of the zonal overturning Indian Walker circulation (Supplementary Fig. 4).

While FGOALS-g1.0 produces strongly enhanced ascent almost everywhere over the Maritime Continent (Fig. 5d), anomalous ascent in CCSM3 is restricted to the western part of the Maritime Continent and the adjacent seas, whereas anomalous subsidence is simulated over the eastern region of the Maritime Continent (Fig. 5b). This scenario agrees with our findings but is at odds with most LGM simulations of the regional tropical circulation and hydroclimate^{11–13}. We infer that during the LGM, convection and rainfall over the western part of the IPWP was stronger than today as a result of a stronger Walker circulation, while further to the east, anomalous subsidence

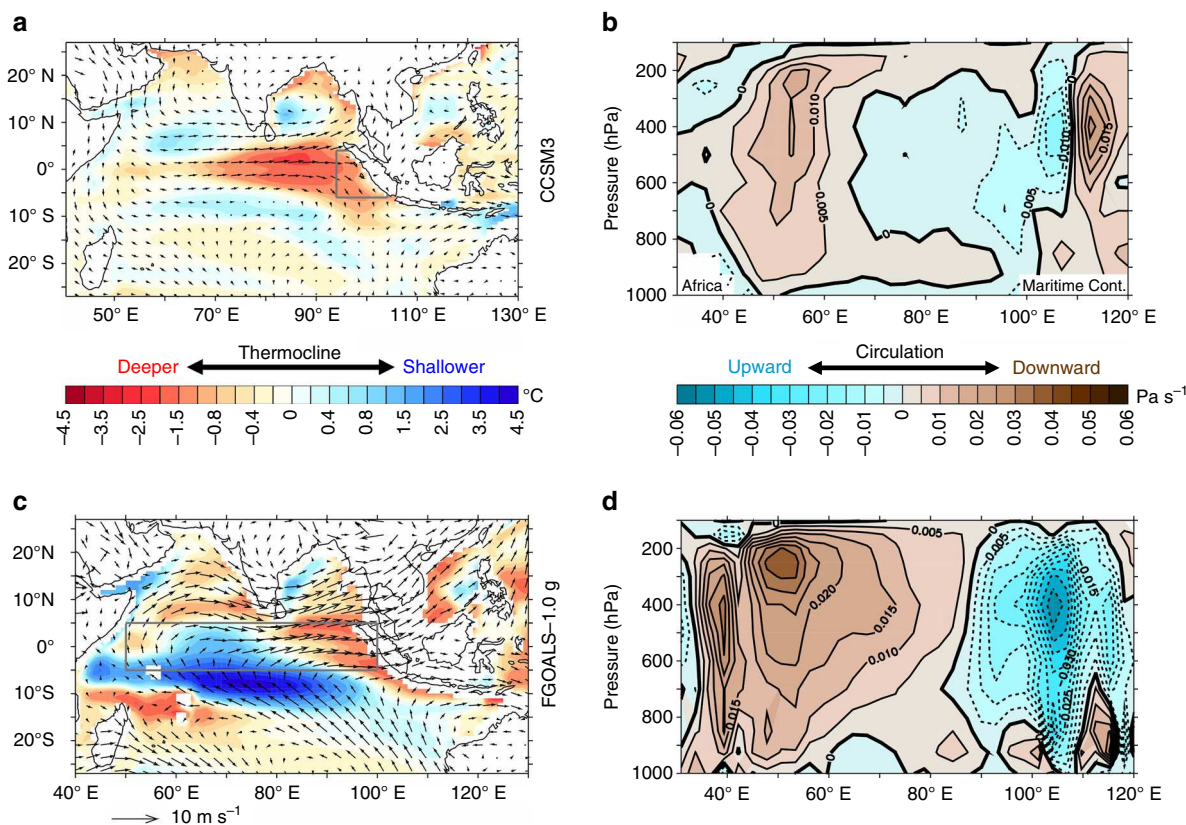


Fig. 5 LGM climate anomalies in the Indian Ocean region as simulated by CCSM3 and FGOALS-g1.0. Shown are LGM anomalies (annual mean) relative to pre-industrial control runs for ΔT (defined as ocean temperature difference between surface and 70 m as a measure for tropical thermocline depth) and low-level (925 hPa) wind (**a, c**) and vertical velocity (ω) between 5° S and 5° N (**b, d**) for the two climate models with greatest LGM thermocline deepening in the eastern equatorial Indian Ocean and strongest equatorial westerly wind anomalies (Nos. 13 and 14 in Fig. 4), CCSM3 (**a, b**) and FGOALS-g1.0 (**c, d**). Grey box in **a** shows the region for calculating area-averaged ΔT in all the models in Fig. 4, while the grey box in **c** shows the region for averaging U_{eq} . Modern coastlines are drawn in **a** and **c** for better orientation

resulted in drier conditions over the Maritime Continent, as indicated by various proxy and model studies (cf. ref. ¹³).

In our model analysis, we show that the depth of the tropical eastern Indian Ocean thermocline is well correlated with the equatorial zonal wind strength and hence a reliable indicator for changes in the Indian Ocean Walker circulation (Fig. 4). In an earlier study¹², the strength of the LGM Indian Ocean Walker circulation was inferred from a compilation of hydroclimate proxies in the Indo-Pacific region and comparison to PMIP model output. There, model agreement with the proxies was quantified by using a Cohen's κ statistic, which is defined as the observed fractional agreement relative to the probability of random agreement. Surprisingly, we find that there is no significant correlation ($r^2 = 0.36$, $p > 0.05$) between LGM zonal wind anomalies over the equatorial Indian Ocean and the degree of model-proxy agreement for rainfall reconstructions as quantified by the published maximum Cohen's κ (Supplementary Fig. 5). The same holds true for sea surface salinity reconstructions compiled in the same study ($r^2 = 0.25$, $p > 0.05$).

Besides the fact that modelling the Maritime Continent rainfall is generally a challenge for climate models³⁶, we surmise that three major factors are responsible for the absence of correlation between the synthesized hydroclimate reconstruction and the Indian Ocean Walker circulation: firstly, the proxy data set considered previously^{12, 13} comprises a too large region (25° S–20° N, 25° E–170° E) containing many sites that are outside the influence of the Indian Ocean Walker cell; secondly, at many sites contained in the proxy compilation rainfall is controlled by

orographic effects not resolved in the relatively coarse-resolution PMIP climate models, e.g. along the mountainous areas of western Sumatra that receive moisture from the Indian Ocean²²; hence, regional-scale rainfall patterns are generally simulated with low skill-level in global climate models; lastly, several proxies included in those compilations^{12, 13} are not straightforwardly related to local precipitation rate. For instance, surface salinity and rainfall decrease in the eastern tropical Indian Ocean during a weak Walker circulation year, and increase during a strong Walker circulation year, while salinity does not change considerably in the western Indian Ocean in both years¹⁵, thus questioning the feasibility of salinity as a reliable measure of rainfall changes.

Our results from two robust proxies for wind strength and precipitation changes from sites beneath the ascending branch of the Indian Ocean Walker cell are at odds with most of the IPWP climate simulations for the LGM^{10, 23}. However, our model-data approach provides a scenario that reconciles the discrepancy in the data and model results of the present and past hydroclimate in this region. Moreover, the inferred scenario of a weaker Walker circulation during the late Holocene from our proxy records, as also simulated by CCSM3 and FGOALS-g1.0, is similar to the projected changes of the Walker circulation over the Indian Ocean during the 21st century greenhouse warming^{1, 37}. We note that several forcings besides temperature were different during the LGM compared to the late Holocene, such as ice sheet and insolation, and require further numerical experiments studying the impact of each of these forcings on Walker circulation

changes. Despite different forcing factors, our results provide evidence for the theoretically projected changes in the strength of the tropical circulation during the 21st century^{2, 3} and suggest that the zonal circulation will further slow down with continued warming. Finally, a weaker Indian Walker circulation as recorded in our data resembles a positive Indian Ocean Dipole state and supports the projected increase in the frequency of extreme positive IOD events in the 21st century, implying severe impacts on hydroclimate around the Indian Ocean and beyond³⁷.

Methods

Sampling and chronology. Piston cores SO189-119KL (3° 31' N, 96° 19' E; 780 cm core length, 808 m water depth) and SO189-39KL (0° 47' S, 99° 54' E; 1350 cm core length, 517 m water depth) were collected from offshore Sumatra during the R/V SONNE cruise 189 in 2006. Gravity cores GeoB 10038-4 (5° 56' S, 103° 15' E, 901 cm core length, 1819 m water depth) and GeoB 10053-7 (8° 41' S, 112° 52' E, 750 cm core length, 1375 m water depth) were collected from the southern Mentawai Basin offshore southwest Sumatra (10038-4) and off southeast Java (10053-7) during the R/V SONNE cruise 184 in 2005. Piston core SO189-39KL was sampled at 2 cm steps; piston core SO189-119KL and gravity cores GeoB 10038-4 and GeoB 10053-7 at 5 cm steps. Core GeoB 10053-7 was additionally sampled at 2 cm steps between 400 cm and 750 cm core depth corresponding to 22–8 kyr BP²⁸. For this study, only the LGM (19–23 kyr) and the late Holocene (0–3 kyr) sections of these cores are considered. Age models of the cores were published previously^{27–29}. The LGM (late Holocene) sections contain 2 (2) radiocarbon datings in SO189-119KL²⁹, 7 (9) in SO189-39KL²⁹, 1 (1) in GeoB 10038-4³⁸ and 3 (3) in GeoB 10053-7²⁸. Sedimentation rates during the LGM and the late Holocene are similar in SO189-119KL (~20 cm kyr⁻¹), in SO189-39KL (~40 cm kyr⁻¹) and in GeoB 10038-4 (~10 cm kyr⁻¹). Sedimentation rates during the LGM (late Holocene) are around 40 (60) cm kyr⁻¹ in GeoB 10053-7.

Planktic foraminifera and thermocline reconstruction. All cores used in this study lie above the calcite lysocline and contain well-preserved aragonitic pteropods that suggest a negligible effect of dissolution on planktic foraminifera shell geochemistry. Previous studies on surface sediments²⁴ and sediment trap time-series³⁹ from the eastern tropical Indian Ocean suggest that mean calcification depth for the mixed-layer dwelling species *Globigerinoides ruber* is about 20 m. Mean calcification depths of the thermocline species have been estimated in the same studies at about 75 m for *Pulleniatina obliquiloculata*, at 75–95 m for *Neoglobobulimina dutertrei* and at about 100 m for *Globorotalia tumida*. Three out of eight temperature records have been published previously^{27–29}. For Mg/Ca analyses, a minimum of 30 *G. ruber* specimens from the 250 to 355 μm size-fraction and a minimum of 20 specimens of the remaining species from the 355 to 500 μm size-fraction have been selected, crushed and cleaned following a slightly modified protocol of Barker et al.⁴⁰ with five water and two methanol washes, two oxidation steps with 1% NaOH-buffered H₂O₂ and a weak acid leach with 0.001 M quartz distilled (QD) HNO₃. Samples were then dissolved into 0.075 M QD HNO₃ and centrifuged for 10 min at 6000 r.p.m., transferred into test tubes and diluted. Mg/Ca ratios in samples from core GeoB 10038-4 and GeoB 10053-7 were measured with a Perkin Elmer Optima 3300R Inductively Coupled Plasma Optical Emission Spectrophotometer (ICP-OES) equipped with an auto sampler and an ultrasonic nebulizer U-5000 AT (Cetac Technologies Inc.). Mg/Ca ratios in samples from core SO189-39KL were measured with an Agilent Technologies 700 Series ICP-OES with a CETAX ASX-520 auto sampler. Both facilities are housed at the Faculty of Geosciences, University of Bremen. Mg/Ca values are reported as mmol mol⁻¹. Instrumental precision was determined using an external, in-house standard (Mg/Ca = 2.92 mmol mol⁻¹) and the ECRM 752-1 standard⁴¹, which were run after every fifth and fiftieth sample, respectively. Relative standard deviations for the external standard, ECRM 752-1 standard, and replicate measurements are listed in Supplementary Table 1. Cleaning efficiency was monitored by measuring Fe/Ca, Mn/Ca and Al/Ca ratios (<0.1 mmol mol⁻¹ for Mn/Ca and Fe/Ca, and not detectable for Al/Ca). Mg/Ca ratios were converted to temperature using the following equations:

For *G. ruber*⁴²:

$$\text{Mg/Ca (mmol mol}^{-1}\text{)} = 0.38 \exp^{(0.09 \cdot T \text{ } ^\circ\text{C})} \quad (1)$$

For *P. obliquiloculata*⁴²:

$$\text{Mg/Ca (mmol mol}^{-1}\text{)} = 0.328 \exp^{(0.09 \cdot T \text{ } ^\circ\text{C})} \quad (2)$$

For *N. dutertrei*⁴²:

$$\text{Mg/Ca (mmol mol}^{-1}\text{)} = 0.342 \exp^{(0.09 \cdot T \text{ } ^\circ\text{C})} \quad (3)$$

For *G. tumida*²⁴:

$$\text{Mg/Ca (mmol mol}^{-1}\text{)} = 0.41 \exp^{(0.068 \cdot T \text{ } ^\circ\text{C})} \quad (4)$$

The use of other calibrations would change the absolute values but not the pattern of change that is central to this study, as demonstrated in Fig. 2. Core-top studies from hypersaline regions such as the Mediterranean Sea with salinities

above 36 psu suggest that the Mg/Ca ratio in planktic foraminifera shells is additionally controlled by salinity⁴³. Data from the IPWP core tops do not show a salinity effect on Mg/Ca as the 36 psu threshold is out of reach in this rain-laden region⁴⁴. Errors (1σ) were calculated following Gibbons et al.⁴⁴ and Mohtadi et al.²⁹, and the 95% confidence intervals are based on *t*-distributed samples in each time interval and indicated by vertical bars (Fig. 1a, Supplementary Data 1).

Results from modern samples corroborate the use of the difference between the Mg/Ca-based temperatures of a surface- and a thermocline-dweller (ΔT) for reconstructing changes in the thermocline depth. This difference in the sediment trap time-series JAM1-2 deployed off south Java³⁹ is smallest during the northwest monsoon season (~2 °C), when high precipitation is accompanied by a warm and deep thermocline³⁹. In contrast, the largest difference (~5 °C) occurs when the thermocline is shallow and cool during the dry southeast monsoon season³⁹. Likewise, Mg/Ca-based temperature estimates in 70 surface sediment samples from this region show that the ΔT between *G. ruber* and *P. obliquiloculata* or *N. dutertrei* follows changes in the stratification of the water column and consequently, the thermocline depth²⁴.

Plant wax analyses. We measured three sediment samples per core and period to average internal variability within each time slice (Supplementary Data 1). About 10 g of dried and ground sediments were extracted with a Dionex Accelerated Solvent Extractor (ASE-200) at 100 °C and 1000 psi with a mixture of dichloromethane/methanol (9:1) for 5 min, which was repeated three times. Squalane was added before extraction as internal standard. Asphaltenes were removed from the total lipid extracts (TLEs) by elution with hexane over Na₂SO₄. TLEs were saponified by 6% KOH in methanol and acid fractions removed. Neutral fractions were separated into aliphatic (apolar), ketone and polar fractions on a silica gel column. Afterwards the aliphatic fraction was separated on an AgNO₃-impregnated silica-column into saturated and unsaturated fractions, of which the first fraction contains the *n*-alkanes. Quantification of *n*-alkanes was performed by gas-chromatography–flame ionization detection (GC–FID) on a ThermoFisher Scientific Focus gas chromatograph. Alkanes were identified and quantified by comparison of retention times and peak areas with an external standard mixture. Repeated analyses of the external standard mixture yield a quantification uncertainty of <5%. The *n*-C₃₁ alkane was the most abundant homologue in all samples. Concentrations varied from 90 to 640 ng g⁻¹ dry sed. and were consistently higher in LGM than Holocene samples (ED 5–6). The carbon preference index (CPI) was calculated to:

$$\text{CPI} = 0.5 * \left(\frac{\sum C_{\text{odd}27-33}}{\sum C_{\text{even}26-32}} + \frac{\sum C_{\text{odd}27-33}}{\sum C_{\text{even}28-34}} \right) \quad (5)$$

with C_x the amount of each homologue⁴⁵.

CPI values of individual samples varied between 2.6 and 6.8 (Supplementary Data 1). On average, the CPI values for the LGM time-slices were higher than for the Holocene samples at each site (Fig. 3). In conjunction, sedimentary concentrations and CPI values indicate a higher contribution of undegraded, i.e. directly plant-derived, long-chain *n*-alkanes to the LGM sediments compared to the Holocene.

Hydrogen isotope compositions were analysed on a ThermoFisher Scientific Trace gas chromatograph connected to a ThermoFisher Scientific MAT 253 mass spectrometer via a pyrolysis reactor operated at 1420 °C. Isotope values were measured against calibrated H₂ reference gas. δD values are reported in ‰ relative to VSMOW. The H³⁺ factor was determined daily and varied around 6.23 ± 0.04 ppm nA⁻¹ during analyses. An alkane standard of 16 externally calibrated alkanes was measured after every 6th measurement. Long-term precision and accuracy of the external alkane standard were 3 and <1‰, respectively. All samples were run at least in duplicate. δD values of the *n*-C₃₁ alkane varied from -150 to -174 ‰ (Supplementary Data 1). Reproducibility for the *n*-C₃₁ alkane was on average 1‰ (<1 to 4‰). Precision and accuracy of the squalane internal standard were 6 and 4‰, respectively (*n* = 34). Mean values and average standard deviation of δD values were calculated for each time slice and are reported within 95% confidence intervals. We correct δD values for global seawater isotopic changes during the LGM. The ice volume correction⁴⁶ was converted to δD values using the global meteoric water line⁴⁷. The ice-volume correction shifts the δD values during the LGM by -9.1‰.

Model simulations. To test the relation between glacial anomalies in zonal equatorial winds and thermocline depth in the Indian Ocean we use LGM and pre-industrial coupled climate model simulations from PMIP2 and PMIP3/CMIP5^{10, 23}. LGM boundary conditions include reduced greenhouse gases, changed astronomical parameters, continental ice sheets and a changed land–sea mask in accordance with a ~120 m lower global sea level compared to today (see <https://pmip2.lscce.ipsl.fr> and <https://pmip3.lscce.ipsl.fr> for details). See Supplementary Table 2 for climate models used in PMIP2 and PMIP3/CMIP5. All model analyses are based on climatological annual means.

Data availability. The authors declare that the data supporting the findings of this study are available within the paper and its supplementary information files. Data can also be downloaded at <https://doi.pangaea.de/10.1594/PANGAEA.877994>

Received: 14 April 2017 Accepted: 31 July 2017

Published online: 18 October 2017

References

- Cai, W. et al. Projected response of the Indian ocean dipole to greenhouse warming. *Nat. Geosci.* **6**, 999–1007 (2013).
- Vecchi, G. A. & Soden, B. J. Global warming and the weakening of the tropical circulation. *J. Clim.* **20**, 4316–4340 (2007).
- Held, I. M. & Soden, B. J. Robust responses of the hydrological cycle to global warming. *J. Clim.* **19**, 5686–5699 (2006).
- Vecchi, G. A. et al. Weakening of tropical Pacific atmospheric circulation due to anthropogenic forcing. *Nature* **441**, 73–76 (2006).
- Tokinaga, H., Xie, S.-P., Deser, C., Kosaka, Y. & Okumura, Y. M. Slowdown of the Walker circulation driven by tropical Indo-Pacific warming. *Nature* **491**, 439–443 (2012).
- Luo, J.-J., Sasaki, W. & Masumoto, Y. Indian Ocean warming modulates Pacific climatic change. *Proc. Natl Acad. Sci.* **109**, 18701–18706 (2012).
- Wang, B. et al. Northern Hemisphere summer monsoon intensified by mega-El Niño/southern oscillation and Atlantic multidecadal oscillation. *Proc. Natl Acad. Sci.* **110**, 5347–5352 (2013).
- L'Heureux, M. L., Lee, S. & Lyon, B. Recent multidecadal strengthening of the Walker circulation across the tropical Pacific. *Nat. Clim. Change* **3**, 571–576 (2013).
- England, M. H. et al. Recent intensification of wind-driven circulation in the Pacific and the ongoing warming hiatus. *Nat. Clim. Change* **4**, 222–227 (2014).
- Braconnot, P. et al. Results of PMIP2 coupled simulations of the Mid-Holocene and Last Glacial Maximum—part 1: experiments and large-scale features. *Clim. Past* **3**, 261–277 (2007).
- DiNezio, P. N. et al. The response of the Walker circulation to Last Glacial Maximum forcing: Implications for detection in proxies. *Paleoceanography* **26**, PA3217 (2011).
- DiNezio, P. N. & Tierney, J. E. The effect of sea level on glacial Indo-Pacific climate. *Nat. Geosci.* **6**, 485–491 (2013).
- DiNezio, P. N. et al. The climate response of the Indo-Pacific warm pool to glacial sea level. *Paleoceanography* **31**, 866–894 (2016).
- Webster, P. J., More, A. M., Loschnigg, J. P. & Leban, R. R. Coupled ocean-atmosphere dynamics in the Indian Ocean during 1997–1998. *Nature* **401**, 356–360 (1999).
- Qiu, Y., Cai, W., Li, L. & Guo, X. Argo profiles variability of barrier layer in the tropical Indian Ocean and its relationship with the Indian Ocean Dipole. *Geophys. Res. Lett.* **39**, L08605 (2012).
- Saji, N. H., Goswami, B. N., Vinayachandran, P. N. & Yamagata, T. A dipole mode in the tropical Indian Ocean. *Nature* **401**, 360–363 (1999).
- Deshpande, A., Chowdhury, J. S. & Gnanaseelan, C. Role of thermocline–SST coupling in the evolution of IOD events and their regional impacts. *Clim. Dyn.* **43**, 163–174 (2014).
- Saji, N. H. & Yamagata, T. Possible impacts of Indian Ocean Dipole mode events on global climate. *Clim. Res.* **25**, 151–169 (2003).
- Rozanski, K., Araguás-Araguás, L. & Gonfiantini, R. in *Climate Change in Continental Isotopic Records* 1–36 (American Geophysical Union, 1993).
- Sachse, D. et al. Molecular paleohydrology: interpreting the hydrogen-isotopic composition of lipid biomarkers from photosynthesizing organisms. *Annu. Rev. Earth Planet. Sci.* **40**, 221–249 (2012).
- Schefuß, E., Schouten, S. & Schneider, R. R. Climatic controls on central African hydrology during the past 20,000 years. *Nature* **437**, 1003–1006 (2005).
- Wu, P., Hara, M., Hamada, J.-I., Yamanaka, M. D. & Kimura, F. Why a large amount of rain falls over the sea in the vicinity of Western Sumatra Island during nighttime. *J. Appl. Meteorol. Climatol.* **48**, 1345–1361 (2009).
- Harrison, S. P. et al. Evaluation of CMIP5 palaeo-simulations to improve climate projections. *Nat. Clim. Change* **5**, 735–743 (2015).
- Mohtadi, M. et al. Reconstructing the thermal structure of the upper ocean: insights from planktic foraminifera shell chemistry and alkenones in modern sediments of the tropical eastern Indian Ocean. *Paleoceanography* **26**, PA3219 (2011).
- Locarnini, R. A. et al. *World Ocean Atlas 2009, Volume 1: Temperature* NOAA Atlas NESDIS 68 (U.S. Government Printing Office, 2010).
- Lückge, A. et al. Monsoon versus ocean circulation controls on paleoenvironmental conditions off southern Sumatra during the past 300,000 years. *Paleoceanography* **24**, PA1208 (2009).
- Mohtadi, M. et al. Late Pleistocene surface and thermocline conditions of the eastern tropical Indian Ocean. *Quat. Sci. Rev.* **29**, 887–896 (2010).
- Mohtadi, M. et al. Glacial to Holocene swings of the Australian-Indonesian monsoon. *Nat. Geosci.* **4**, 540–544 (2011).
- Mohtadi, M. et al. North Atlantic forcing of tropical Indian Ocean climate. *Nature* **509**, 76–80 (2014).
- Qu, T., Du, Y., Strachan, J., Meyers, G. & Slingo, J. M. Sea surface temperature and its variability in the Indonesian region. *Oceanography* **18**, 50–62 (2005).
- Susanto, R. D. & Marra, J. Effect of the 1997/1998 El Niño on Chlorophyll *a* variability along the southern coasts of Java and Sumatra. *Oceanography* **18**, 124–128 (2005).
- Romero, O. E., Mohtadi, M., Helmke, P. & Hebbeln, D. High interglacial diatom paleoproductivity in the westernmost Indo-Pacific Warm Pool during the past 130,000 years. *Paleoceanography* **27**, PA3209 (2012).
- Song, Q. & Gordon, A. L. Significance of the vertical profile of the Indonesian throughflow transport on the Indian Ocean. *Geophys. Res. Lett.* **31**, L16307 (2004).
- Niedermeyer, E. M., Sessions, A. L., Feakins, S. J. & Mohtadi, M. Hydroclimate of the western Indo-Pacific Warm Pool during the past 24,000 years. *Proc. Natl Acad. Sci.* **111**, 9402–9406 (2014).
- Hamilton, W. B. *Tectonics of the Indonesian region*. Report No. 1078, 345 (U.S. Geological Survey, 1979).
- Christensen, J. H. et al. in *Climate Change 2013: The Physical Science Basis. Contribution of Working Group I to the Fifth Assessment Report of the Intergovernmental Panel on Climate Change* (eds Stocker, T. F., et al.) (Cambridge University Press, 2013).
- Cai, W. et al. Increased frequency of extreme Indian ocean dipole events due to greenhouse warming. *Nature* **510**, 254–258 (2014).
- Mohtadi, M., Steinke, S., Lückge, A., Groenewald, J. & Hathorne, E. C. Glacial to Holocene surface hydrography of the tropical eastern Indian Ocean. *Earth Planet. Sci. Lett.* **292**, 89–97 (2010).
- Mohtadi, M. et al. Low-latitude control on seasonal and interannual changes in planktonic foraminiferal flux and shell geochemistry off south Java: a sediment trap study. *Paleoceanography* **24**, PA1201 (2009).
- Barker, S., Greaves, M. & Elderfield, H. A study of cleaning procedures used for foraminiferal Mg/Ca paleothermometry. *Geochem., Geophys., Geosyst.* **4**, 8407 (2003).
- Greaves, M. et al. Interlaboratory comparison study of calibration standards for foraminiferal Mg/Ca thermometry. *Geochem., Geophys., Geosyst.* **9**, Q08010 (2008).
- Anand, P., Elderfield, H. & Conte, M. H. Calibration of Mg/Ca thermometry in planktonic foraminifera from a sediment trap time series. *Paleoceanography* **18**, 1050 (2003).
- Ferguson, J. E., Henderson, G. M., Kucera, M. & Rickaby, R. E. M. Systematic change of foraminiferal Mg/Ca ratios across a strong salinity gradient. *Earth Planet. Sci. Lett.* **265**, 153–166 (2008).
- Gibbons, F. T. et al. Deglacial $\delta^{18}\text{O}$ and hydrologic variability in the tropical Pacific and Indian Oceans. *Earth Planet. Sci. Lett.* **387**, 240–251 (2014).
- Bray, E. E. & Evans, E. D. Distribution of *n*-paraffins as a clue to recognition of source beds. *Geochim. Cosmochim. Acta* **22**, 2–15 (1961).
- Waelbroeck, C. et al. Sea-level and deep water temperature changes derived from benthic foraminifera isotopic records. *Quat. Sci. Rev.* **21**, 295–305 (2002).
- Craig, H. Isotopic variations in meteoric waters. *Science* **133**, 1702–1703 (1961).
- Cléroux, C. et al. Mg/Ca and Sr/Ca ratios in planktonic foraminifera: proxies for upper water column temperature reconstruction. *Paleoceanography* **23**, PA3214 (2008).

Acknowledgements

We are grateful to A. Lückge, B. Meyer-Schack, M. Segl, H. Kuhnert, R. De Pol-Holz, R. Kreutz, S. Pape, K. Gesierich, M. Baumer and B. Beckmann for laboratory assistance. This study was supported by the Bundesministerium für Bildung und Forschung through grants 03G0184A (PABESIA), 03G0189A (SUMATRA), 03G0806B (CARIMA) and the PalMod initiative, and the Deutsche Forschungsgemeinschaft (grants JE281/4-1, HE3412/15-1, and the DFG Research Centre/Cluster of Excellence ‘The Ocean in the Earth System’). We acknowledge the World Climate Research Programme’s Working Group on Coupled Modelling, which is responsible for CMIP, and the climate modelling groups (listed in Supplementary Table 2) for producing and making available their model output. For CMIP the U.S. Department of Energy’s Program for Climate Model Diagnosis and Intercomparison provides coordinating support and led development of software infrastructure in partnership with the Global Organization for Earth System Science Portals. The Laboratoire des Sciences du Climat et de l’Environnement (LSCE) is acknowledged for collecting and archiving the PMIP2 model data. The PMIP2 Data Archive is supported by CEA, CNRS and the Programme National d’Etude de la Dynamique du Climat (PNEDC).

Author contributions

M.M. and E.S. generated and analysed the data, M.P. analysed the climate model experiments. M.M. and T.C.J. designed the study and all authors discussed and interpreted the data.

Additional information

Supplementary Information accompanies this paper at [10.1038/s41467-017-00855-3](https://doi.org/10.1038/s41467-017-00855-3).

Competing interests: The authors declare no competing financial interests.

Reprints and permission information is available online at <http://npg.nature.com/reprintsandpermissions/>

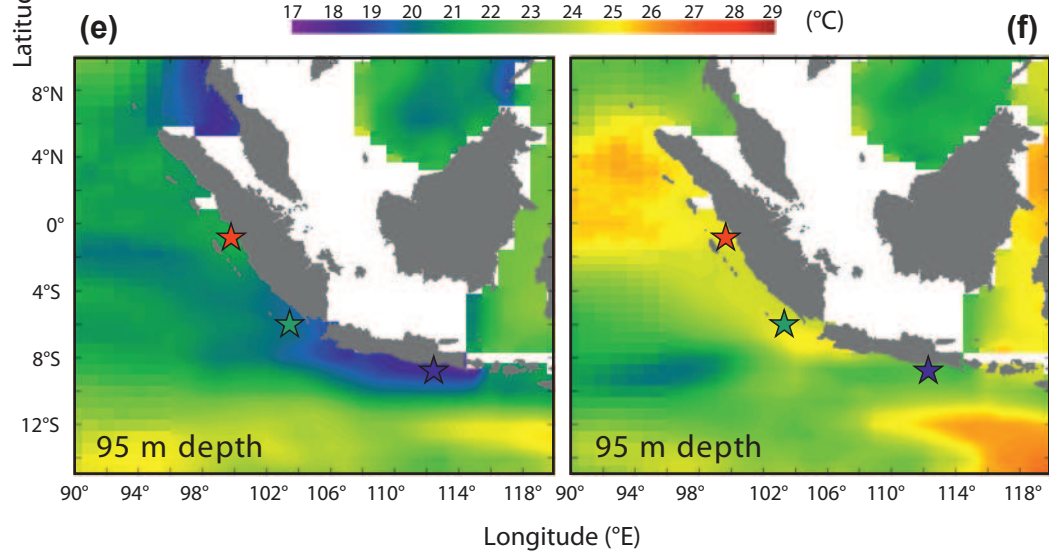
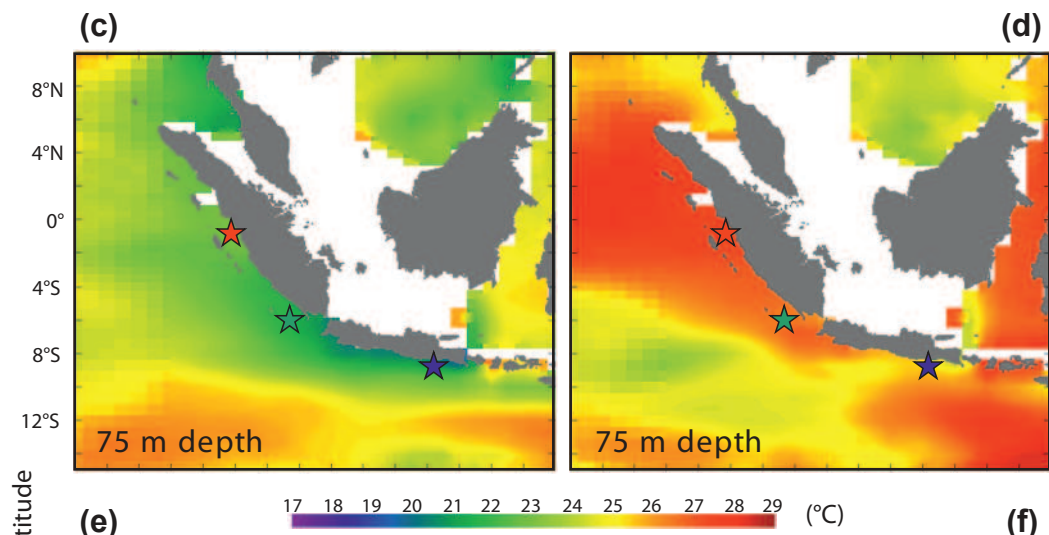
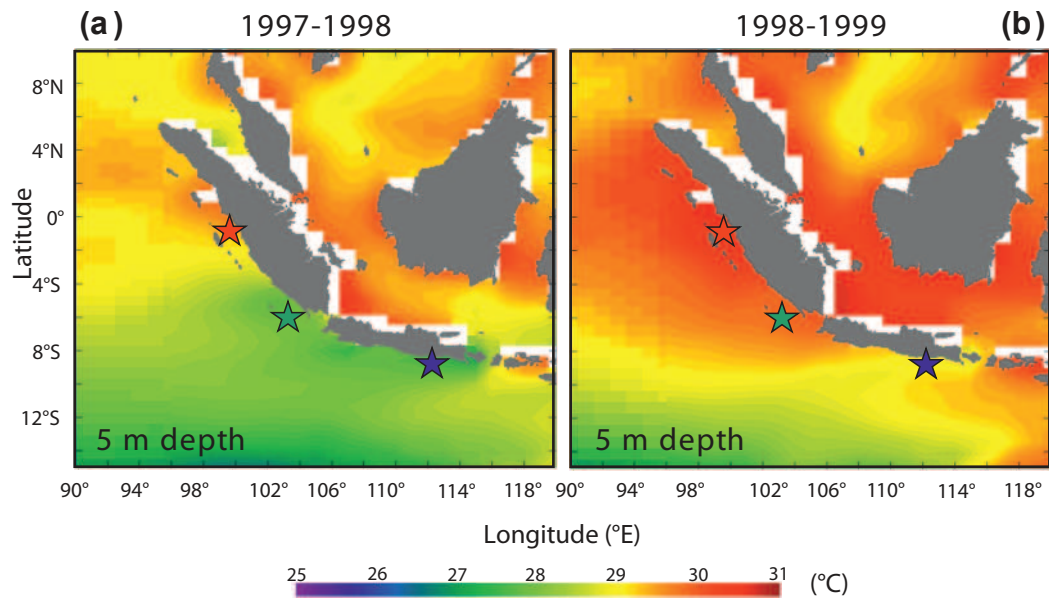
Publisher's note: Springer Nature remains neutral with regard to jurisdictional claims in published maps and institutional affiliations.

adaptation, distribution and reproduction in any medium or format, as long as you give appropriate credit to the original author(s) and the source, provide a link to the Creative Commons license, and indicate if changes were made. The images or other third party material in this article are included in the article's Creative Commons license, unless indicated otherwise in a credit line to the material. If material is not included in the article's Creative Commons license and your intended use is not permitted by statutory regulation or exceeds the permitted use, you will need to obtain permission directly from the copyright holder. To view a copy of this license, visit <http://creativecommons.org/licenses/by/4.0/>.

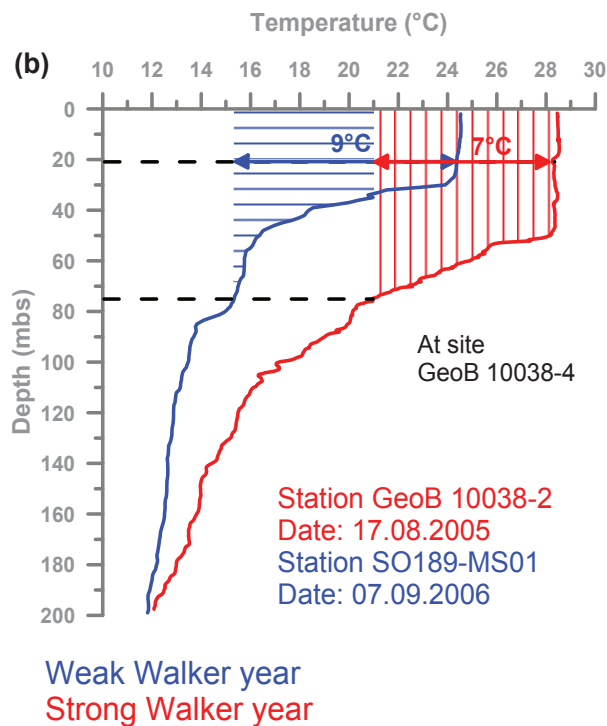
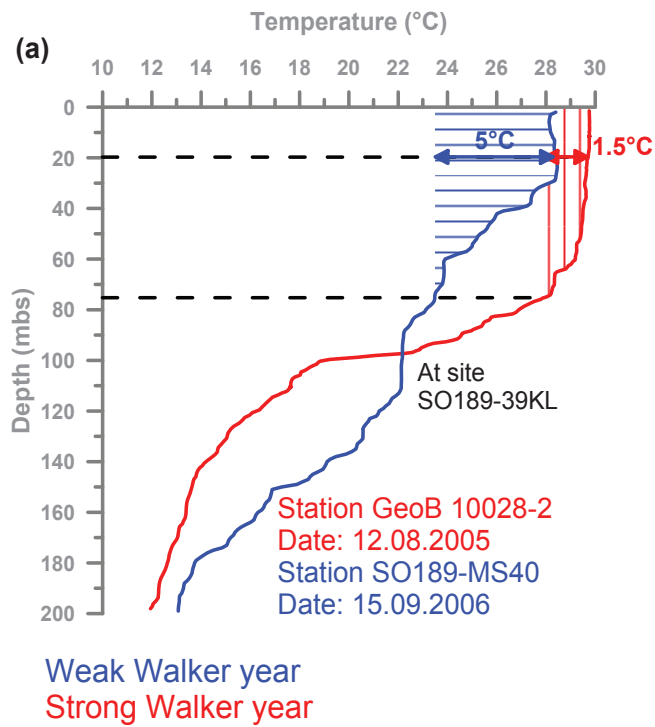
© The Author(s) 2017



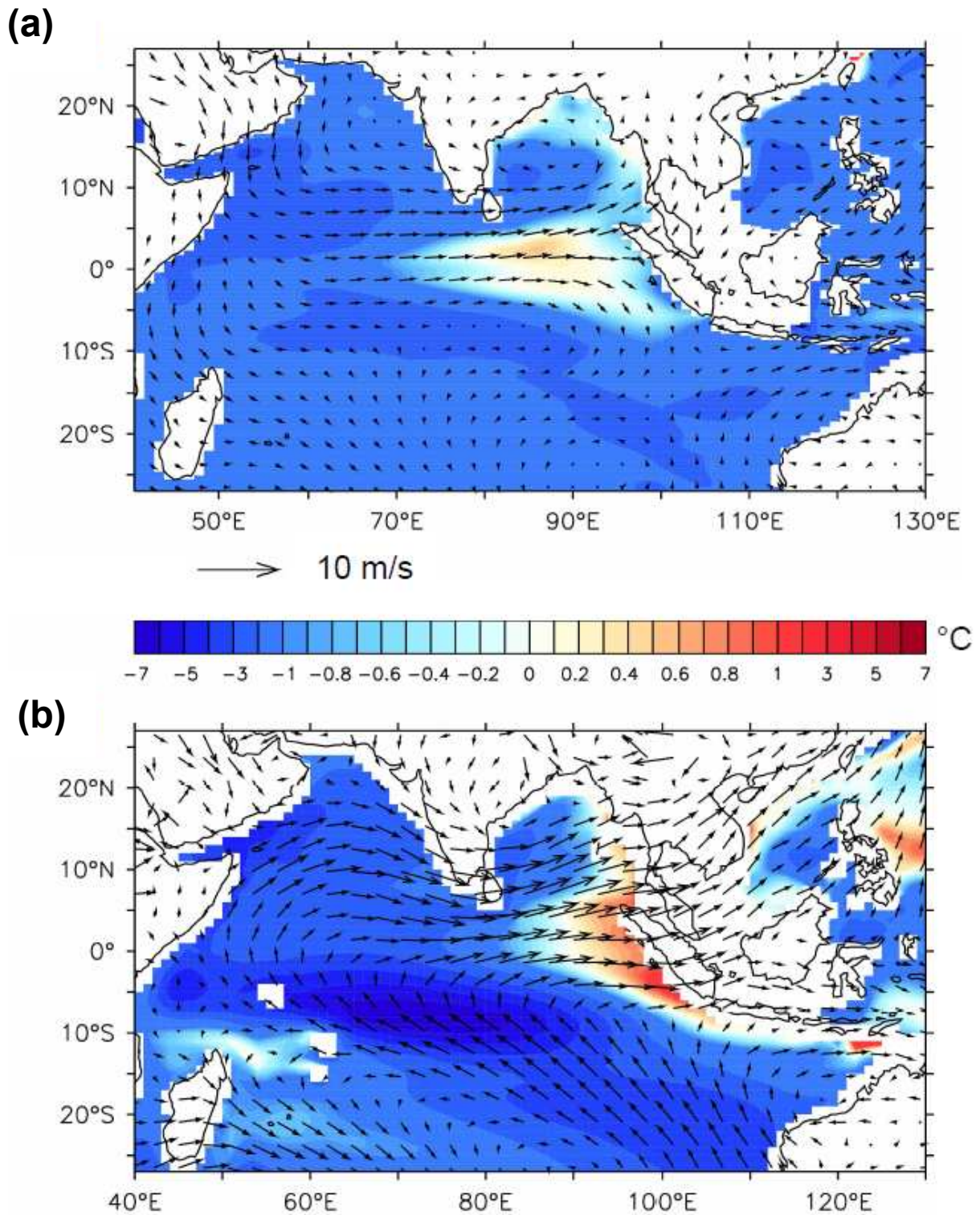
Open Access This article is licensed under a Creative Commons Attribution 4.0 International License, which permits use, sharing,



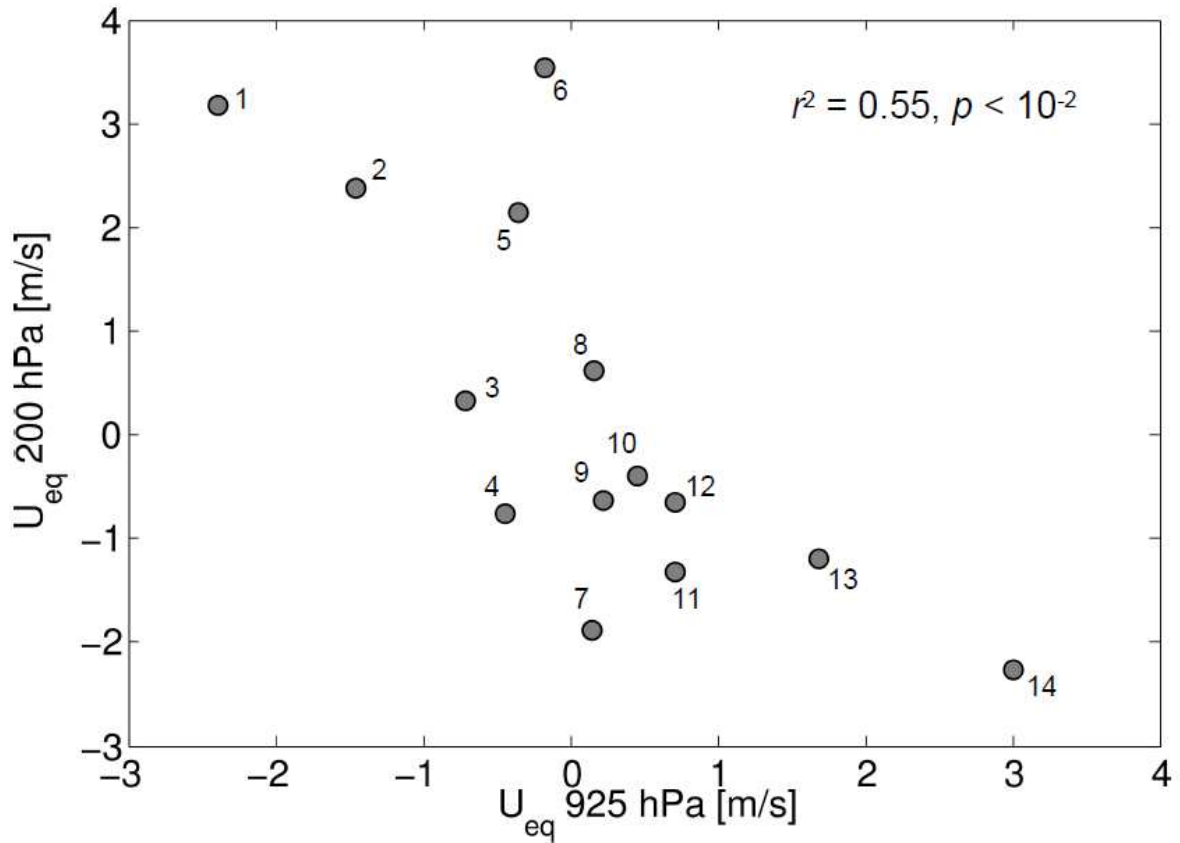
Supplementary Figure 1. Modern changes in mean annual surface and thermocline temperatures of the eastern tropical Indian Ocean. Potential temperature at **(a, b)** 5 m water depth, **(c, d)** 75 m water depth, and **(e, f)** at 95 m water depth during a positive Indian Ocean Dipole - El Niño year from March 16, 1997 to March 16, 1998 **(a, c, e)** and a La Niña year from March 16, 1998 to March 16, 1999 **(b, d, f)**. Note the different scale for **(a, b)**. Data from <http://data1.gfdl.noaa.gov>. Stars indicate the position of the records presented in this study (red: 39KL, green: GeoB 10038-4, blue: GeoB 10053-7). Note the observed warming in a strong Walker circulation scenario (right) compared to a weak Walker circulation scenario (left).



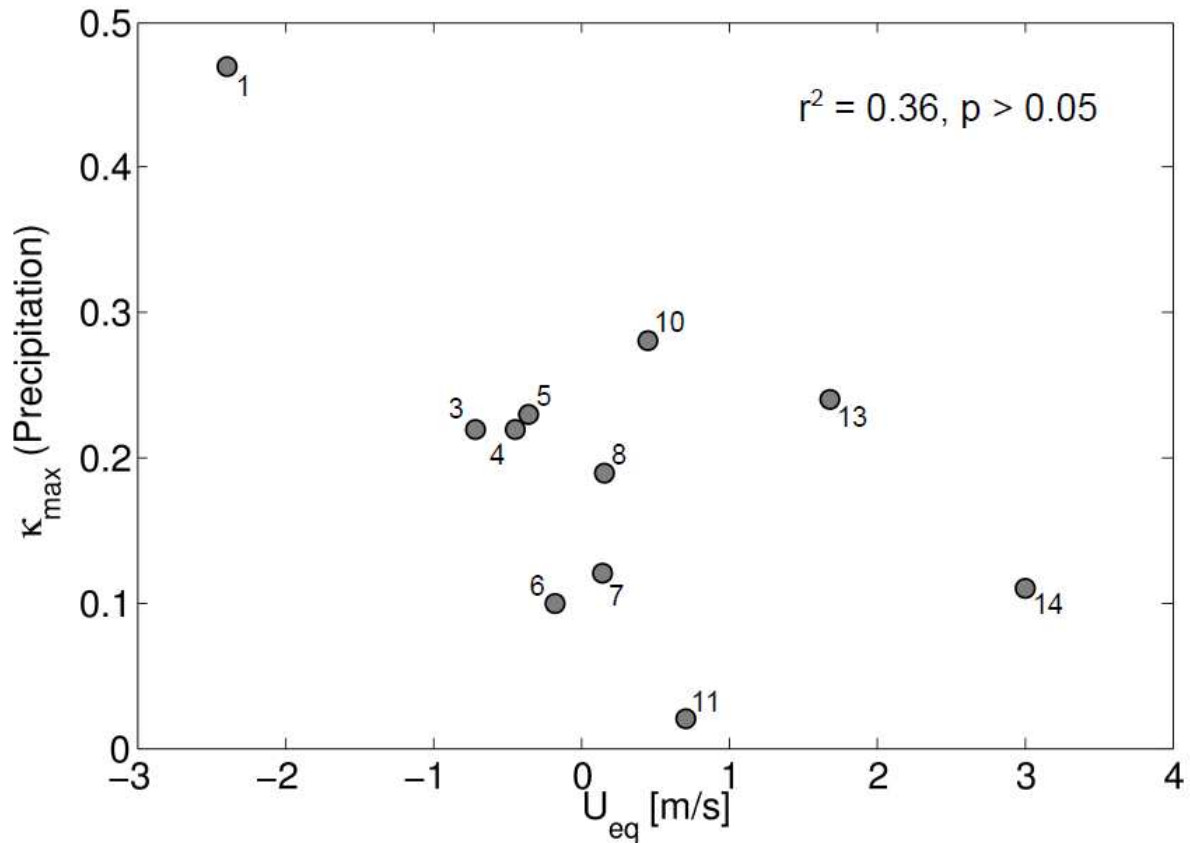
Supplementary Figure 2. Response of the water column structure in the eastern tropical Indian Ocean to changes in Walker circulation. CTD data from a strong Walker circulation year (2005, red) and a weak Walker circulation year (2006, blue) at sites (a) SO189-39KL and (b) GeoB 10038-4. Note the deeper and warmer thermocline during the strong Walker year. Double-headed arrows and coloured strips show the temperature difference (ΔT) between 20 m and 75 m water depth indicated by dashed lines. Note the smaller ΔT during the strong Walker year.



Supplementary Figure 3. LGM ocean subsurface warming in CCSM3 and FGOALS-g1.0. Shown are LGM anomalies (annual mean) relative to pre-industrial control runs for the 70 m temperature for **(a)** CCSM3 and **(b)** FGOALS-g1.0. Low-level wind anomalies and coastlines as in Fig. 5.



Supplementary Figure 4. Upper-tropospheric (200 hPa) zonal wind anomalies versus low-level (925 hPa) zonal wind anomalies over the equatorial Indian Ocean as simulated in PMIP2 and PMIP3/CMIP5 models. Zonal wind anomalies, U_{eq} , are defined as the annual mean zonal wind averaged over 5°N-5°S, 50°E-100°E (see Fig. 5), LGM relative to pre-industrial. The models are numbered as in Supplementary Table 2.



Supplementary Figure 5. Maximum Cohen's κ versus equatorial Indian Ocean zonal wind anomaly as simulated in PMIP models. U_{eq} is defined as the LGM anomaly (relative to pre-industrial) of the annual mean zonal low-level (925 hPa) wind averaged over 5°N-5°S, 50°E-100°E (see Fig. 5). Maximum Cohen's κ has been used to quantify model-data agreement with respect to precipitation proxies in the Indo-Pacific region, for the calculation of Cohen's κ see¹. The models are numbered as in Supplementary Table 2. Three models (No. 2, 9, and 12) were not included in (ref¹), hence no κ values are available.

Core/Species	# Samples	# Replicates	1 σ Standard Deviation (mmol mol ⁻¹)		
			Ext. standard	ECRM 752-1	Replicates
SO189-39KL					
<i>G. ruber</i>	671	55	0.005	0.006	0.12
<i>P. obliquiloculata</i>	651	50	0.004	0.003	0.10
GeoB 10038-4					
<i>G. ruber</i>	184	39	0.09	0.009	0.09
<i>P. obliquiloculata</i>	60	26	0.09	0.009	0.22
<i>N. dutertrei</i>	248	94	0.09	0.009	0.25
<i>G. tumida</i>	62	25	0.09	0.009	0.11
GeoB 10053-7					
<i>G. ruber</i>	291	30	0.01	0.01	0.19
<i>P. obliquiloculata</i>	271	30	0.02	0.01	0.21

Supplementary Table 1. Amount and relative standard deviation of Mg/Ca measurements at different sites. Standard deviations (1 σ) for external standard and ECRM 752-1 are calculated by considering all measurements during a analytical campaign as indicated in the column “# Samples”. Standard deviation for replicates refers to measurements on additional samples that have been separately cleaned and measured (column “# Replicates”), and then compared to their corresponding samples from the original run (column # Samples).

No.	Model	Institution	Grid resolution	PMIP phase
1	HadCM3	UK Met Office Hadley Centre, UK	Atm: 96 x 72 x L19 Ocn: 288 x 144 x L20	2
2	FGOALS-g2.0	LASG/Institute of Atmospheric Physics, China	Atm: 128 x 60 x L26 Ocn: 360 x 180 x L30	3
3	IPSL-CM4	Institut Pierre Simon Laplace, France	Atm: 96 x 72 x L19 Ocn: 182 x 149 x L31	2
4	CNRM-CM5	Centre National de Recherches Meteorologiques, France	Atm: 256 x 128 x L31 Ocn: 362 x 292 x L42	3
5	GISS-E2-R	NASA Goddard Institute for Space Studies, USA	Atm: 144 x 90 x L40 Ocn: 288 x 180 x L32	3
6	IPSL-CM5A	Institut Pierre Simon Laplace, France	Atm: 96 x 96 x L39 Ocn: 182 x 149 x L31	3
7	MRI-CGCM3	Meteorological Research Institute, Japan	Atm: 320 x 160 x L48 Ocn: 364 x 368 x L51	3
8	MIROC3.2	Center for Climate System Research (University of Tokyo), JAMSTEC, Japan	Atm: 128 x 64 x L20 Ocn: 256 x 192 x L43	2
9	ECHAM5-MPIOM	Max Planck Institute for Meteorology, Germany	Atm: 96 x 48 x L19 Ocn: 120 x 101 x L40	2
10	MPI-ESM	Max Planck Institute for Meteorology, Germany	Atm: 196 x 98 x L47 Ocn: 256 x 220 x L40	3
11	CCSM4	National Center for Atmospheric Research, USA	Atm: 288 x 192 x L26 Ocn: 320 x 384 x L60	3
12	MIROC-ESM	JAMSTEC, University of Tokyo, National Inst. for Environmental Studies, Japan	Atm: 128 x 64 x L80 Ocn: 256 x 192 x L44	3
13	CCSM3	National Center for Atmospheric Research, USA	Atm: 128 x 64 x L26 Ocn: 320 x 384 x L40	2
14	FGOALS-g1.0	LASG/Institute of Atmospheric Physics, China	Atm: 128 x 60 x L26 Ocn: 360 x 180 x L33	2

Supplementary Table 2. PMIP2 and PMIP3/CMIP5 models providing LGM and pre-industrial simulations used in this study. In the column for grid resolution the following abbreviations are used: Atm (atmospheric grid resolution), Ocn (ocean grid resolution), L (number of levels in the vertical). The numbering (first column) is related to the simulated magnitude of LGM zonal wind anomalies over the equatorial Indian Ocean and used in Fig. 4 and Supplementary Figs. 4-5. For further references regarding the climate models the reader is referred to <https://pmip2.lsce.ipsl.fr> and <https://pmip3.lsce.ipsl.fr>.

Supplementary references

- 1 DiNezio, P. N. & Tierney, J. E. The effect of sea level on glacial Indo-Pacific climate. *Nature Geoscience* **6**, 485-491, doi:10.1038/ngeo1823 (2013).